A&A 664, A168 (2022)
https://doi.org/10.1051/0004-6361/202243762

Astronomy & Astrophysics

Ca II triplet spectroscopy of Small Magellanic Cloud red giants

VI. Analysis of chemical properties of the main body*

B. J. De Bortoli[1,2,3], M. C. Parisi[3,4,5], L. P. Bassino[1,2,3], D. Geisler[6,7,8], B. Dias[9], G. Gimeno[10], M. S. Angelo[11], and F. Mauro[12]

[1] Facultad de Cs. Astronómicas y Geofísicas, Universidad Nacional de La Plata, Paseo del Bosque s/n, 1900 La Plata, Argentina
e-mail: brudebo.444@gmail.com
[2] Instituto de Astrofísica de La Plata (CCT La Plata, UNLP-CONICET), Paseo del Bosque s/n, 1900 La Plata, Argentina
[3] Consejo Nacional de Investigaciones Científicas y Técnicas, Godoy Cruz 2290, C1425FQB Ciudad Autónoma de Buenos Aires, Argentina
[4] Observatorio Astronómico de Córdoba, Universidad Nacional de Córdoba, Laprida 854, X5000BGR Córdoba, Argentina
[5] Instituto de Astronomía Teórica y Experimental (UNC-CONICET), Laprida 854, X5000BGR Córdoba, Argentina
[6] Departamento de Astronomia, Casilla 160-C, Universidad de Concepcion, 4030000 Concepción, Chile
[7] Instituto de Investigación Multidisciplinario en Ciencia y Tecnología, Universidad de La Serena, Avenida Raúl Bitrán s/n, La Serena, Chile
[8] Departamento de Astronomía, Facultad de Ciencias, Universidad de La Serena, Av. Juan Cisternas 1200, 1720236 La Serena, Chile
[9] Instituto de Alta Investigación, Sede Esmeralda, Universidad de Tarapacá, Av. Luis Emilio Recabarren 2477, 1100000 Iquique, Chile
[10] Gemini Observatory, NSF's NOIRLab, 950 N. Cherry Ave., Tucson, AZ 85719, USA
[11] Centro Federal de Educação Tecnológica de Minas Gerais, 38778-000 Minas Gerais, Brazil
[12] Instituto de Astronomía, Universidad Católica del Norte, 127 0236 Antofagasta, Chile

Received 12 April 2022 / Accepted 30 May 2022

ABSTRACT

Aims. In this paper we analyze the chemical evolution of the main body of the SMC, adding six additional clusters to previously published samples, based on homogeneously determined and accurate metallicities.
Methods. We derived radial velocities and Ca II Triplet (CaT) metallicity of more than 150 red giants stars in six SMC star clusters and their surrounding fields, with the instrument GMOS on GEMINI-S. The mean cluster radial velocity and metallicity were obtained with mean errors of 2.2 km s^{-1} and 0.03 dex, while the mean field metallicities have a mean error of 0.13 dex. We add this information to that available for another 51 clusters and 30 fields with CaT metallicities on the same scale. Using this expanded sample we analyze the chemical properties of the SMC main body, defined as the inner 3.4° in semimajor axis.
Results. We found a high probability that the metallicity distribution of the main body clusters is bimodal with a metal-rich and a metal-poor cluster group, having mean metallicities with a dispersion of $\mu = -0.80$, $\sigma = 0.06$ and $\mu = -1.15$, $\sigma = 0.10$ dex, respectively. On the other hand, main body field stars show a unimodal metallicity distribution peaking at [Fe/H] ~ -1 and dispersion of 0.3. Neither metal-rich nor metal-poor clusters present a metallicity gradient. However, the full main body cluster sample and field stars have a negative metallicity gradient consistent with each other, but the one corresponding to clusters has a large error due to the large metallicity dispersion present in the clusters studied in that region. Metal-rich clusters present a clear age–metallicity relation, while metal-poor clusters present no chemical enrichment throughout the life of the galaxy.
Conclusions. We present observational evidence that the chemical enrichment is complex in the SMC main body. Two cluster groups with potential different origins could be coexisting in the main body. More data with precise and homogeneous metallicities and distances are needed and dynamical simulations are required to understand the possible different origins for the two cluster groups.

Key words. galaxies: star clusters: general – Magellanic Clouds – stars: abundances

1. Introduction

The Magellanic System (D'Onghia & Fox 2016) is one of the most rewarding nearby systems for the study of dwarf galaxies and the stellar populations that they host. It consists of the Small Magellanic Cloud (SMC), the Large Magellanic Cloud (LMC), the Bridge, the Magellanic Stream and the Leading Arm. The SMC and LMC are the closest pair of interacting galaxies to the Milky Way (MW) located at distances of 49.59 ± 0.09 kpc (Pietrzyński et al. 2019) and 62.44 ± 0.47 kpc (Graczyk et al. 2020), respectively. The Magellanic Clouds (MCs) are embedded within a diffuse structure of HI gas (Mathewson et al. 1974; Putman et al. 2003; Nidever et al. 2008, 2010), which has been interpreted by numerous works as the consequence of interaction either between the SMC and LMC or among the SMC, LMC and the MW (e.g., Diaz & Bekki 2011, 2012; Besla et al. 2012, 2016). There is some discussion in the literature as to whether MCs have been orbiting the MW (Gardiner & Noguchi 1996; Diaz & Bekki 2012); however the latest research based

* Full Table 2 is only available at the CDS via anonymous ftp to cdsarc.u-strasbg.fr (130.79.128.5) or via http://cdsarc.u-strasbg.fr/viz-bin/cat/J/A+A/664/A168

on the most accurate measurements of proper motions with the *Hubble* Space Telescope (HST) and *Gaia*, and updated LMC and MW mass estimates, suggests that they are experiencing their first encounter with our Galaxy (Besla et al. 2007, 2010; Piatek et al. 2008; Kallivayalil et al. 2013; Patel et al. 2017; Gaia Collaboration 2018).

Regardless of whether the MCs are experiencing their first encounter with the MW or not, it is expected that the morphologies of the two galaxies are being modified by tidal interactions (Martin et al. 2021). The dynamical simulations carried out in recent years (e.g. Connors et al. 2006; Bekki & Chiba 2007; Diaz & Bekki 2012; Besla et al. 2012), have been able to reproduce many of the morphological characteristics of the Magellanic System (Magellanic Stream, Leading Arm, Magellanic Bridge, Counter-Bridge) as a consequence of the interaction between the MCs. A large number of studies have found evidence of tidal tails around the SMC and the LMC (Besla et al. 2007; Belokurov & Erkal 2019; Nidever et al. 2019; Gaia Collaboration 2021; El Youssoufi et al. 2021; Dias et al. 2021). In particular, the complex patterns of velocities in the SMC, found for example by Niederhofer et al. (2018, 2021), suggest that this galaxy is being tidally disrupted by the LMC. The current morphology of the SMC could also be the consequence of a recent collision between the MCs (Besla et al. 2012; Zivick et al. 2018).

Given such interactions, the star formation histories and chemical enrichment processes of the stellar populations of a galaxy are affected (Whitmore et al. 1999; Da Costa 1991; Dopita et al. 1997; Pagel & Tautvaisiene 1998). Their spatial, age, and metallicity distributions and gradients present distinctive effects of the interaction processes (e.g., Cioni 2009; Dobbie et al. 2014a; Nayak et al. 2016; Dias et al. 2016; Rubele et al. 2018; De Leo et al. 2020; Santos et al. 2020). SMC star clusters have historically proven to be excellent tracers of the chemical and dynamical history of this galaxy (e.g., Da Costa & Hatzidimitriou 1998; Glatt et al. 2010; Parisi et al. 2009, 2014, 2015; Perren et al. 2017; Piatti 2018; Nayak et al. 2018; Bitsakis et al. 2018; Narloch et al. 2021; Dias et al. 2021). However, despite the exhaustive study of the chemical properties of the SMC clusters, there is some controversy in the literature regarding the chemical evolution of this galaxy using those objects as tracers.

Several studies have shown that the field metallicity distribution (MD) is unimodal with a [Fe/H] maximum near −1 dex (e.g., Carrera et al. 2008; Parisi et al. 2010; Dobbie et al. 2014b; Parisi et al. 2016; Choudhury et al. 2018, 2020). However, using a sample of 36 clusters homogeneously studied, Parisi et al. (2015, hereafter P15) suggest that the MD could be bimodal with a probability of 86%. This probability drops drastically to 59% when the cluster sample increases significantly (Parisi et al. 2022, hereafter P22), but nevertheless the sample shows a marked absence of clusters in the internal region with metallicity values typical of the SMC field.

Although there is agreement in most studies regarding the existence of a metallicity gradient (MG) in the SMC field (e.g., Carrera et al. 2008; Parisi et al. 2010, 2016; Dobbie et al. 2014b; Choudhury et al. 2018, 2020), it is not clear if the SMC clusters present such a gradient. Narloch et al. (2021) studied 35 clusters with Strömgren photometry and they found that younger, more metal-rich star clusters are concentrated mainly towards the centre of the galaxy, while older more metal-poor clusters are located farther from the centre. However, studies based on CaII triplet (CaT) metallicities from Parisi et al. (2009, hereafter P09), P15, Dias et al. (2022, hereafter D22), and P22 find that although there is a tendency for the clusters to be more metal-poor as we move away from the center of the galaxy up to 4°, the cluster MG is not statistically significant due to the large cluster metallicity dispersion in the internal region (∼0.6 dex, P15, P22). To make things more interesting, employing the separation of SMC cluster samples into the different sky regions defined by Dias et al. (2016, 2021, hereafter D16, D21), we can see that the clusters belonging to the Northern Bridge appear to be the ones that best trace a V shape in the MD (P22, D22), and the West Halo clusters could present a MG (D16, D22), but with some uncertainty (P22).

This metallicity dispersion, observed in spectroscopic studies and also in photometric studies (e.g., Perren et al. 2017; Narloch et al. 2021), is also evident in the analyzed age–metallicity relation (AMR) in which the models of chemical evolution proposed in the literature for the SMC do not reproduce the data in general (Da Costa & Hatzidimitriou 1998; Harris & Zaritsky 2004; Pagel & Tautvaisiene 1998; Carrera et al. 2008; Cignoni et al. 2013; Tsujimoto & Bekki 2009; Perren et al. 2017). The V shape present in the field and metallicity gradient (P15, P16, Bica et al. 2020, D16) is under discussion, especially in the outer region where it is not clear whether the gradient increases or remains constant (Parisi et al. 2016; Choudhury et al. 2020, P22, D22).

Galaxy-galaxy interactions are expected to mostly affect the outskirts of the SMC (Mayer et al. 2001), but D22 show that the SMC disruption due to tidal effects starts much farther inside the SMC tidal radius (Dias et al. 2021). In addition, P22 showed that all the components suggested by D21 present a minimum in metallicity as well as smaller metallicity dispersion near the projected tidal radius. Significantly different cluster chemical properties are displayed by samples inside versus outside the tidal radius. The outer cluster system of the SMC is being systematically studied by the VISCACHA survey (Maia et al. 2019) with results that impose important constraints on dynamical models of the Magellanic Clouds (D21, D22). In this paper we focus our analysis on the internal region, where chemical evolution does not seem to follow a canonical behavior.

We organized the paper as follows. In Sect. 2 we describe the cluster sample selection, observations, and data reduction process. The measurement of radial velocities and equivalent width of the Ca II Triplet lines and the metallicity determination are presented in Sect. 3. Sections 4 and 5 are dedicated to the membership and metallicity analysis, respectively. Finally we summarize our results in Sect. 6.

2. Observations and data reduction

In order to increase the number of inner SMC star clusters homogeneously studied with the CaT technique, we observed six clusters in the inner region of the SMC that are spatially distributed, as can be seen in Fig. 1. The ellipses are defined in the plane of relative RA versus relative DEC, with ratio $b/a = 0.5$ and position angle = 45° (Piatti et al. 2005; Dias et al. 2014). The semimajor axis a of the ellipse coincident with the position of the cluster is used as the projected distance from the SMC center. We considered the semimajor axis $a = 3.4°$ as the division between the inner and outer regions of the SMC (D21), so our sample basically consists of clusters in the SMC main body (D16, D21, P22). Clusters were selected from Piatti (2011a,b) and Piatti et al. (2011). We prioritized those clusters whose color-magnitude Diagram (CMD) shows the most populated red giant branch (RGB) in order to maximize the number of suitable targets for the CaT technique. Although our whole sample has ages

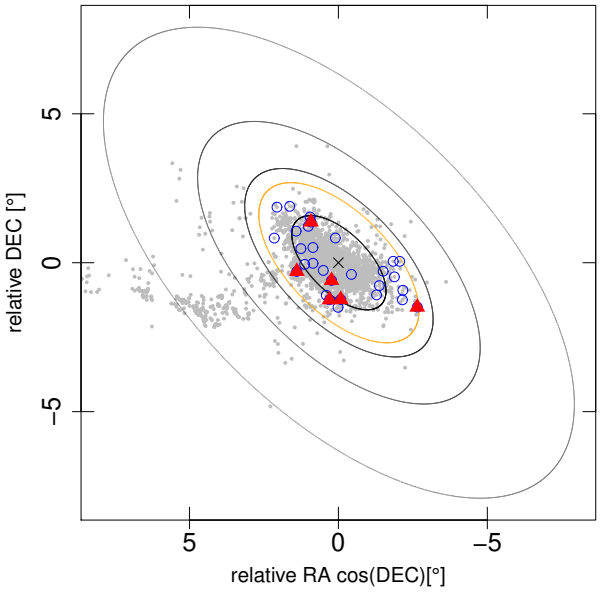

Fig. 1. Projected spatial distribution of SMC star clusters. The gray dots show clusters catalogued by Bica et al. (2020); blue open circles are star clusters taken from the literature (Da Costa & Hatzidimitriou 1998, P09, P15, D21, P22 and D22) and filled red triangles are the clusters studied in this paper. The orange ellipse corresponds to a semimajor axis of 3.4°. The black ellipses correspond to semimajor axes of 2°, 4°, 6° and 10°. They are centered on the SMC, with PA = 45° and $b/a = 1/2$.

and metallicities previously determined from photometric techniques, in this work we provide more accurate spectroscopic metallicities derived from the CaT technique as well as radial velocities (RVs). The cluster sample is presented in Table 1, which includes coordinates, projected distances and ages.

For each cluster, pre-images in the g and r filters had been previously obtained with the instrument Gemini/GMOS-S (program GS-2014B-Q-78), from which the CMDs [g, $g-r$] were built. We selected RGB stars from the CMDs as spectroscopic targets. As an example, we show in Fig. 2 the CMD for the cluster K 38. The spectroscopic targets are shown with large circles in the figure, following the color-coding related to our membership analysis (see the figure caption and Sect. 4 for details).

The spectroscopic data for the selected RGB stars consist of intermediate resolution infrared spectra obtained with GMOS-S (Hook et al. 2004), with the new Hamamatsu CCDs featuring enhanced red sensitivity (Gimeno et al. 2016) in MOS mode (program GS-2016B-Q-17). It comprises more than 150 spectra of stars in the area of our SMC cluster sample. Observations of 4×900 s exposure time and 2×2 binning were taken for each frame, using the R831 disperser and the CaT_G0333 filter. The four observations were taken in pairs centered on 8500 Å and 8550 Å for dithering. On average, 26 slits of 1 arcsec width were located in each frame. This instrumental configuration yields a spectral resolution of 0.075 nm px^{-1} ($R \sim 2000$). Calibration observations, such as bias, flat fields, and CuAr arc spectra, were also taken.

In order to reduce the spectra, we used the script[1] developed by M. Angelo. First, we applied the bias and flat corrections, interpolated across the useless CCD gap (GMOSAIC task), identified the spatial extension of each slitlet (GSCUT task), and cut and pasted the two-dimensional spectra in different FITS file extensions. Additionally, bad pixel masks were applied. The wavelength solution for each individual spectrum was obtained from the GSWAVELENGTH task and differences in quantum efficiency between the three CCD chips were corrected with the GQECORR task. Afterwards, we used CRMEDIAN and FIXPIX to remove cosmic rays. We then ran the GSTRANSFORM task, using arc spectra, to rectify the spectra and apply the appropriate wavelength solution. Finally, we extracted and combined the spectra of different central wavelengths, summing them.

In order to analyze whether a zero point correction to our wavelength calibration was necessary, we measured in our spectra the center of several bright sky lines with well-known central wavelengths (Hanuschik 2003). When a non-negligible difference was found, we used SPECSHIFT to shift the spectra. In all cases the corrections were smaller than 0.4 Å (~14 km s^{-1}), except for the cluster K 38 for which it was necessary to apply a shift of 0.9 Å (~32 km s^{-1}).

Finally, we ran the CONTINUUM task to normalize the spectra to the pseudo-continuum level (e.g., Vásquez et al. 2015). As an example, we show in Fig. 3 two normalized spectra of RGB stars in two clusters with very similar evolutionary stages but different metallicities. The signal-to-noise ratio (S/N) for combined and normalized spectra range from 50 to 130.

3. Stellar parameter determination

3.1. Radial velocity and equivalent width measurements

The determination of target radial velocities (RVs) is crucial for cluster membership determination. They are also needed to perform the Doppler correction in order to measure equivalent widths (EWs) of the three CaT lines in rest spectra.

In order to measure the RVs of our program stars, we cross-correlated our normalized spectra with a RGB theoretical template taken from the library of Coelho (2014). We selected a template with typical parameters for a RGB star ($T_{\rm eff}$ = 5000 K, $\log(g)$ = 1 dex, [Fe/H] = −1 dex and [α/Fe] = 0.4 dex), and we convolved the spectrum to reach the spectral resolution of GMOS. As was shown by D22, the mean RV does not vary significantly when adopting different templates in the ranges of $T_{\rm eff}$ = 4700 to 5300 K, [Fe/H] = −1.3 to −0.5, and $\log(g)$ = 1, which are typical of the RGB stars.

We used the IRAF task FXCOR to perform the cross-correlation, which additionally corrects the observed RVs providing the heliocentric values. We obtained a typical RV error of ~4 km s^{-1}.

As we describe in the next section, the EWs of the CaT lines are required for the metallicity determination. Following the same procedure as in our previous work (e.g., P09, P15), the pseudo-continuum was fitted in a pair of continuum windows to shorter and longer wavelengths of the corresponding line center, using the line and continuum bandpasses from Armandroff & Zinn (1988). We fitted a Gaussian plus a Lorentzian function to each CaT line, with respect to the pseudo-continuum, and calculated the "pseudo-EW". As shown by Rutledge et al. (1997a,b) and Cole et al. (2004), this combined function adequately takes into account the contribution of the wings and the core of the line profile. We obtained a typical EW error of ~0.08 Å.

3.2. Metalicity determination

Many studies have calibrated the strength of the CaT lines with metallicity from integrated and individual spectra of RGB

[1] http://drforum.gemini.edu/topic/gmos-mos-guidelines-part-1/

Table 1. Selected SMC cluster sample.

Cluster	RA (J2000.0) (h m s)	Dec (J2000.0) (° ′ ″)	a (°)	Age (Gyr)
K 38, L 57	0:57:49.5	−73:25:23	1.363	3.0 ± 0.4[1]
HW 31, [RZ2005] 97	0:55:34.0	−74:3:46	2.149	4.6 ± 0.3[1]
HW 41, [RZ2005] 125	1:00:33.6	−71:27:13	1.769	5.6 ± 0.4[1]
HW 42	1:01:08.0	−74:04:25	2.617	≈2.4[2]
L 3, ESO 28−13, OGLE-CL SMC 323	0:18:25.2	−74:19:05	2.938	1.2 ± 0.3[3]
L 91, [RZ2005] 194	1:12:51.6	−73:07:07	2.609	4.1 ± 0.3[1]

References. [1]Parisi et al. (2014), [2]Bica et al. (in prep.), [3]Dias et al. (2014).

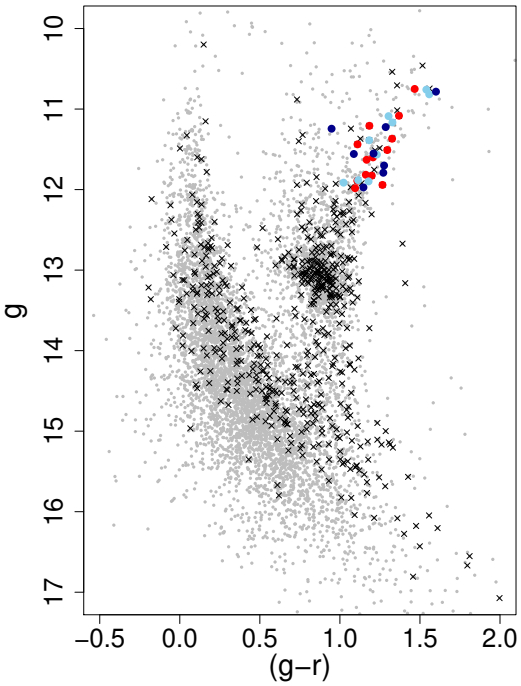

Fig. 2. Color-magnitude diagram of the cluster K 38. The small gray circles show all the objects located in the corresponding frame. The black crosses are the objects located inside the cluster radius. The blue, cyan and green symbols represent targets discarded due to their distance from the cluster center, RV and metallicity, respectively. The red circles are cluster members according to our membership analysis (see Sect. 4 for details).

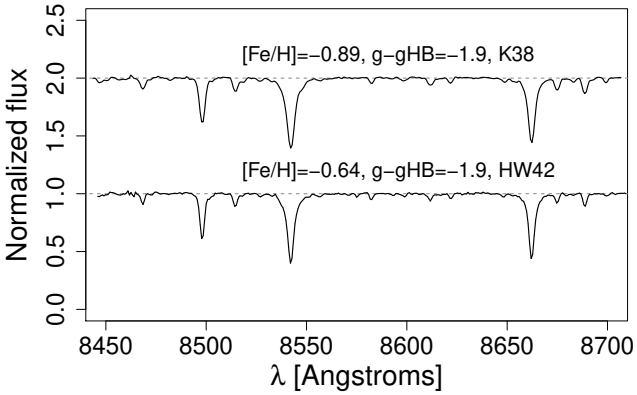

Fig. 3. Normalized GMOS spectra for the clusters K 38 (*top*) and HW 42 (*bottom*).

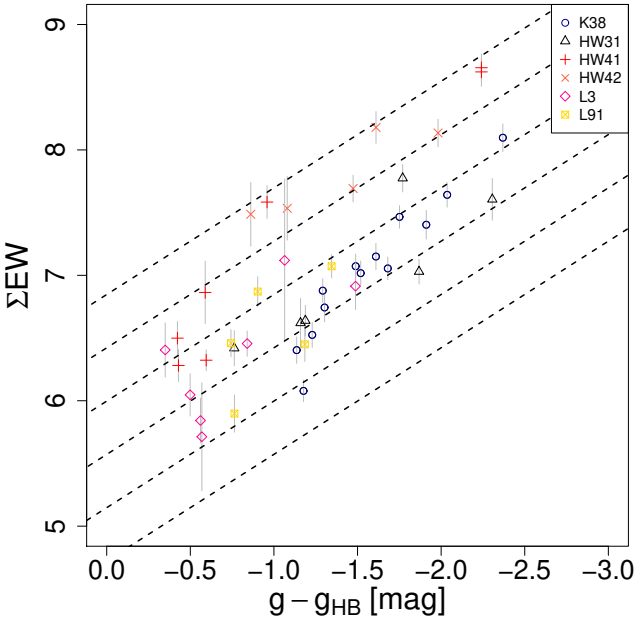

Fig. 4. Sum of the EWs of the three CaT lines against $g-g_{\rm HB}$ for member stars of the six SMC clusters. The dashed lines represent lines of constant metallicity corresponding to [Fe/H] = −0.5, −0.65, −0.80, −0.95, −1.10, and −1.25 dex, *from top to bottom*.

stars. In the case of individual stellar spectra, the technique requires the construction of the CaT index as the sum of the EW of two or three CaT lines (ΣEW). It is also necessary to remove the effects of surface gravity and temperature on the ΣEW (Armandroff & Da Costa 1991; Olszewski et al. 1991), for example by using the difference in magnitudes, in a given filter, between the observed star and the horizontal branch or red clump. A detailed description of the different ways of building the CaT index and the filters used in the literature, as well as the available calibrations, can be found in Dias & Parisi (2020, hereafter DP20) and references therein.

Usually, using the sum of the three CaT lines is the best choice because it takes into account the complete information. However, if the S/N is low, the faintest line mostly adds noise and increases the errors in metallicity, so that it is avoided in these cases, following an adequate calibration. In this work most of the spectra have S/N between 50 and 130, which is high enough to produce good quality CaT lines in almost all cases. Therefore, we use the calibration including the three lines, as follows:

$$\Sigma{\rm EW} = {\rm EW}_{8498} + {\rm EW}_{8542} + {\rm EW}_{8662}. \quad (1)$$

Table 2. Measured parameters for the observed RGB stars.

Star ID	RA (J2000.0) (h m s)	Dec (J2000.0) (° ′ ″)	RV (km s^{-1})	$g - g_{HB}$ (mag)	ΣEW (Å)	[Fe/H] (dex)	Cluster/Field C/F
K 38-2	0:57:49.3	−73:22:45	177.2 ± 4.2	−1.56	7.88 ± 0.13	−0.60 ± 0.21	F
K 38-4	0:58:15.9	−73:26:09	161.7 ± 2.8	−1.57	7.27 ± 0.09	−0.82 ± 0.20	F

Notes. Full table is available at the CDS.

In those cases where the weakest line could not be well fit, we added the contribution of the two most intense lines and then performed the corresponding conversion according to Eq. (5) of DP20. We then calculated the reduced EW (W') as

$$W' = \Sigma EW + \beta(g - g_{HB}) \quad (2)$$

where $(g - g_{HB})$ represents the difference between the magnitude of the star (g) and the magnitude of the cluster's horizontal branch or the red clump (g_{HB}). By considering the magnitude difference, we not only remove the dependence of ΣEW on surface gravity and temperature, but also its dependence on cluster distance and interstellar reddening. We adopt a β value of 0.85 ± 0.08 from DP20, which was calculated for filter g using as reference $\beta_V = 0.71$ for the canonical V filter. We note that this value of β_V is the same used in our previous works, and therefore our measurements are on the same scale.

The g magnitudes were obtained from PSF photometry performed on the pre-images using the SkZ pipeline (Mauro et al. 2013; Mauro 2020). We then determined g_{HB} from the cluster CMD following the procedure detailed in DP20. Figure 4 shows the ΣEW as a function of $g - g_{HB}$ for targets that resulted to be cluster members according to our membership analysis (see Sect. 4). Finally, we calculated the metallicity of each observed star using the calibration derived by DP20:

$$[Fe/H] = -2.917(\pm 0.116) + 0.353(\pm 0.020)W'. \quad (3)$$

As shown by DP20, their calibration is in excellent agreement with the one derived by Cole et al. (2004). Therefore, our metallicity values are on the same scale as our previous work, where Cole's calibration was used. We obtained individual uncertainties on [Fe/H] typically of ∼0.2 dex.

Table 2 presents coordinates and measured values, with their respective errors, for all observed RGB stars. We differentiated the cluster member stars from those belonging to their surrounding fields, according to our membership analysis (see Sect. 4). Stars are labeled with the cluster name plus a number, which represents the aperture number in our program.

4. Membership analysis

In order to separate cluster members from SMC field stars, we followed the same procedure as in our previous work (see P09, P15, and P22 for more details). In summary, for each cluster we first built the radial density profile using stellar counts from our photometry and adopting the cluster center from Bica et al. (2020). The cluster radius is defined as the distance from the center out to the level where the profile intersects the background density, but in some cases we adopted a smaller radius in order to maximize the probability that the selected stars belong to the clusters (Fig. 5). We assume the background level to be that at which the radial profile does not decease significantly any further. The exceptions are the clusters HW 42 and K 38 for which the radial profile could not be constructed due to the low cluster

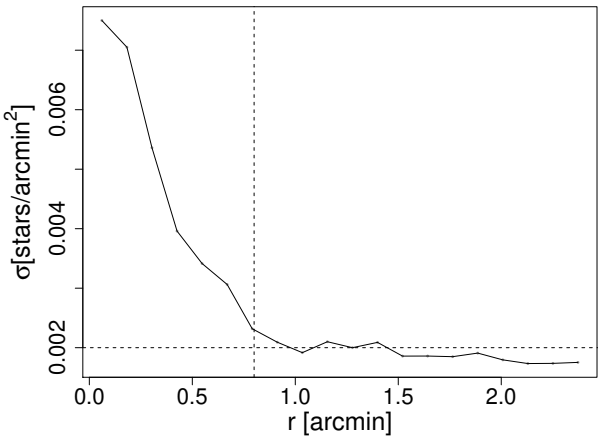

Fig. 5. Radial stellar density profile of the cluster L 91. The horizontal dashed line is the stellar background level; the vertical dashed line shows the adopted cluster radius.

overdensity with respect to the field. In these cases, the radius values from Bica et al. (2020) were adopted. We then analyzed the targets' RV and metallicity as a function of the distance from the cluster center (Fig. 6). Stars closer to the center have a higher probability of being cluster members. It is also assumed that, in general, cluster members have smaller velocity dispersion and potentially different mean RV and metallicity compared to field stars. We adopted the RV and metallicity cuts of ±10 km s^{-1} and ±0.2 dex (from C09, P15 and P22) around the mean value of the visually identified probable member candidates. The RV cuts are consistent with the intrinsic cluster RV dispersion and our mean RV error. The adopted metallicity cuts are representative of our mean metallicity error.

We consider as member stars those targets located closer to the cluster center than the adopted radius and having RV and metallicity values inside the cuts (red symbols in Fig. 6). In the figure, targets discarded as probable cluster members because of their distance, RV, and metallicity values are represented with blue, cyan and green circles, respectively. The RV and metallicity cuts are shown with short dashed lines in Fig. 6 while the adopted cluster radius is represented by the dotted line.

Finally, we checked the proper motions (PMs) of our targets, from the *Gaia* EDR3 (Gaia Collaboration 2021) catalogue, in order to maximize the membership probability of our cluster member candidates. We use the PM to verify that the spectroscopic members have consistent PM values among them. None of the stars considered cluster members according to the criteria described above was discarded due to their PMs.

Using only member stars we calculated the simple mean RV and metallicity for each cluster. As a representative metallicity of the cluster surrounding fields, we calculated the median of non-member stars metallicity values, as suggested by Dobbie et al. (2014b) and Parisi et al. (2016). To determine the median field

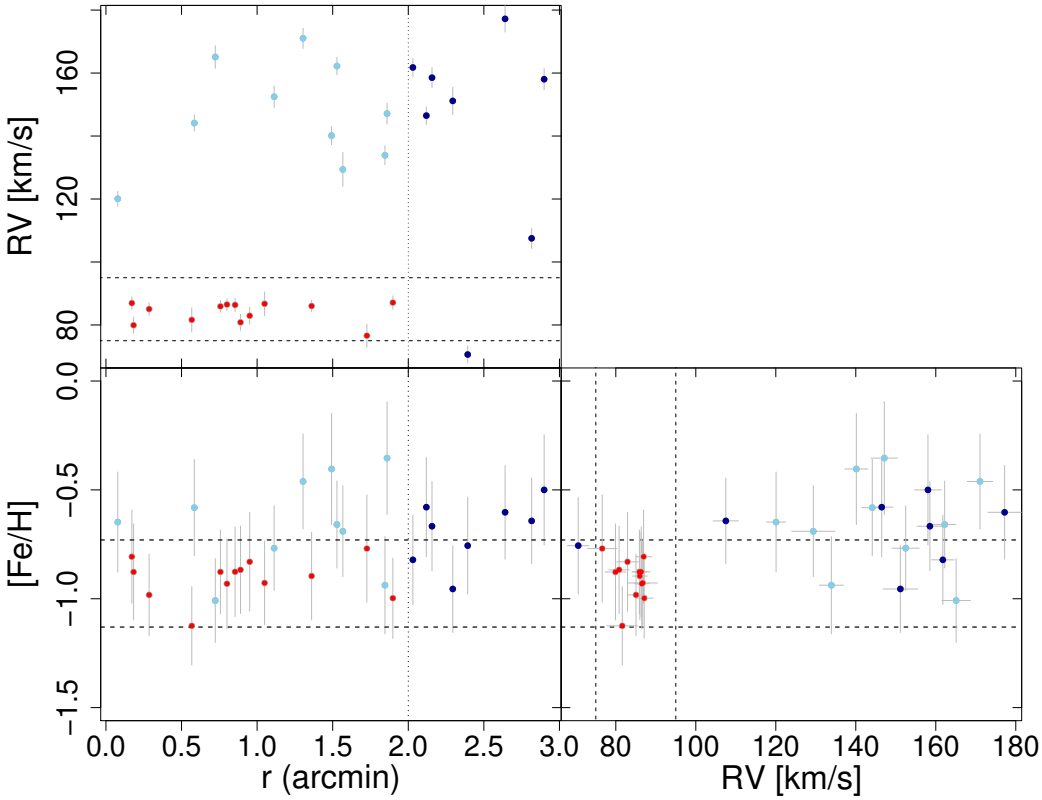

Fig. 6. Membership analysis for the cluster K 38. The color-coding is the same as in Fig. 2. The cluster radius is shown by the dotted vertical line and the dashed lines represent the adopted RV and metallicity cuts.

Table 3. Mean parameters for the selected SMC star clusters and their standard error of the mean.

Cluster	n	RV (km s^{-1})	[Fe/H] (dex)	$n_{\rm field}$	[Fe/H]$_{\rm field}$ (σ) (dex)
K 38	13	84.0 ± 0.9	−0.90 ± 0.02	18	−0.65 ± 0.04 (0.18)
HW 31	6	125.5 ± 3.4	−0.89 ± 0.04	15	−1.12 ± 0.10 (0.37)
HW 41	7	143.6 ± 1.6	−0.67 ± 0.05	14	−0.96 ± 0.10 (0.36)
HW 42	5	144.3 ± 2.0	−0.58 ± 0.03	13	−0.95 ± 0.12 (0.42)
L 3	7	140.1 ± 3.4	−0.90 ± 0.05	3	−0.75 ± 0.37 (0.33)
L 91	5	126.7 ± 1.8	−0.90 ± 0.06	18	−1.01 ± 0.08 (0.35)

metallicities, we verified that the selected stars do not have RV and metallicity values close to the limits imposed by the adopted cuts nor were located close to the cluster radius ($\Delta r <$ 0.2 arcmin, ΔRV $<$ 5 km s^{-1} and Δ[Fe/H] $<$ 0.1 dex). The results for both cluster and field stars are given in Table 3. The median metallicity for the field of L 3 is less reliable because the sample contains only three stars.

5. Chemical properties of cluster and field stars

In order to perform a statistically more significant study of the SMC chemical history, we enlarged our cluster sample by adding 51 clusters having CaT metallicities derived with the same method as in this work: 1 cluster from Da Costa & Hatzidimitriou (1998, hereafter DH98), 15 from P09, 13 from P15, 7 from D21, 12 from P22 and 3 from D22. Out of the seven clusters studied by DH98 we only included here NGC 121. For the rest of the DH98 cluster sample we adopt, for homogeneity, the values derived by P15 and P22, which are in excellent agreement with the CaT metallicities derived by DH98. While P09, P15 and P22 employed data from the VLT-FORS2, the clusters studied in P22 and in this work were observed with Gemini-GMOS. The FORS2 and GMOS samples have two clusters in common (NGC 151 and K 8). The FORS2 metallicity of NGC 151 (P22) is in very good agreement with the GMOS metallicity (D22). In the case of K 8 both datasets (P15 and D22) have four stars in common with metallicities in agreement, one of them a cluster member. Therefore, we consider that the metallicities based on FORS2 and GMOS data are consistent. Then, our final sample includes 57 clusters with metallicities on the same scale spread over all SMC regions of which 37 are in the main body. Hence, the six GCs analyzed in this work represent an increase in the inner SMC cluster sample of 16%.

In addition, we add to our field sample those studied by Parisi et al. (2010, 2016, hereafter P10 and P16). The fields studied in these two works (15 from P10 and 15 from P16) correspond to the fields surrounding the clusters studied in P09 and P15, respectively. Therefore we have a total

of 36 SMC fields with homogeneously determined average metallicities.

5.1. Metallicity distribution

In order to analyze the existence of bimodality in the MD, as suggested by P09 and P15, we applied the Gaussian mixture modeling test (GMM, Muratov & Gnedin 2010) to the full sample. The MD of our cluster sample, as well as the fits considering one (dashed line) or two (dotted lines) Gaussian functions, are shown in Fig. 7. The results for the application of this algorithm are summarized in the first line of Table 4. In the table we list the sample, the peaks (μ) and the standard deviation (σ) for the unimodal and bimodal fits, the p value (which is the probability of incorrectly rejecting unimodality), the bimodality probability given by the parametric bootstrap, the separation of the peaks of the fitted Gaussian functions (DD), and the kurtosis of the distribution (k). An indication of a bimodal distribution is given by a negative k value and $DD > 2$ (Ashman et al. 1994). As can be seen from the table we found a significantly lower probability (39%) than that obtained by P15 (86%) that the whole SMC cluster MD is bimodal, in agreement with P22 (59%).

Considering the different behavior observed for the chemical properties of clusters and field stars in the inner and outer regions, we decided to analyze their MDs separately. We divided our total cluster sample considering clusters inside and outside of 3.4° and applied the GMM test to each of these two subsamples (Table 4). The internal and external MDs can be seen in Figs. 8 and 9, respectively. As can be seen from the results included in the table, while the outer MD presents a probability consistent with that found for the entire sample (∼37%), the inner part shows a high probability of a bimodal MD (∼95%). The inner MD analysis also shows a DD greater than 2 and a negative kurtosis. This means that the possible bimodality in the internal region of the SMC is lost when we analyze the entire sample. The possible existence of bimodality in the inner region suggests the idea of two possible cluster populations coexisting towards the main body having a mean metallicity lower and higher (−1.15 and −0.80 dex, respectively, see Table 4) than the typical mean metallicity of field stars (∼−1, P16). In order to analyze whether the bimodality distribution is an artifact of our sample missing clusters with [Fe/H] ∼ −1 in the inner region, we performed an experiment generating random clusters with [Fe/H] values scattered around −1 dex and with a dispersion of 0.1, and repeated the GMM test. The results show that we had to add 14 clusters (which represents an increase of 37% of the total sample) to bring the probability of bimodality down to 50%. Even in these cases, the DD and the kurtosis remain larger than 2 and negative, respectively. So, we consider that the probability of bimodality being an artifact is low. In the case of the outer MD analysis shows a DD lower than 2 and a positive kurtosis. The metallicities of our extended field star sample clearly show a unimodal distribution (Fig. 10), with a peak at −0.99, in agreement with previous works. Considering these results, we define two groups of clusters in the inner region, which we hereafter call metal-poor and metal-rich clusters. The mean metallicities for the metal-rich and metal-poor clusters are −0.8 and −1.15 dex, respectively, corresponding to the peaks of the bimodal fit of the inner cluster MD (Table 4).

5.2. Metallicity gradient

The behavior of the cluster metallicity as a function of the projected distance to the SMC center a for our cluster sample can

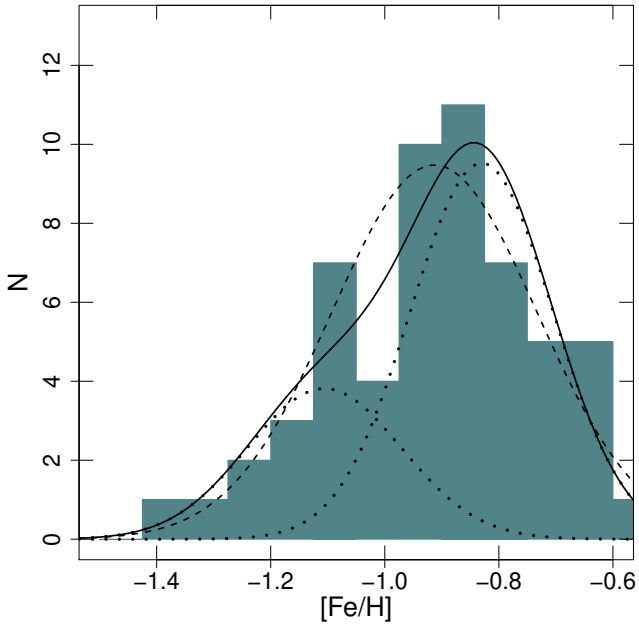

Fig. 7. Metallicity distribution of the enlarged cluster sample. The dotted lines are the two fitted Gaussian functions according to the results from the GMM test and the solid line shows their sum. The dashed line shows the fitted Gaussian in the unimodal case.

be seen in the upper panel of Fig. 11. The field MG is shown for comparison in the middle panel of that figure while the lower panel shows the difference between field and cluster metallicities. This last panel has been included to analyze the suggestions of P10 and P16 that most clusters are more metal-rich than the corresponding fields, which can be observed for the inner clusters in the figure. This implies that the metallicity gradient of the clusters is shifted with respect to that of the field towards higher metallicities, with the exception of clusters of the metal-poor group.

Following the analysis of our previous work, we determined from our extended samples the MGs in the inner and outer regions of the galaxy (solid lines in Fig. 11). We found values of -0.08 ± 0.04 dex deg^{-1} and 0.03 ± 0.02 dex deg^{-1} for the inner and outer regions of the cluster sample, respectively. With respect to field stars, the linear fits give a MG of -0.08 ± 0.03 dex deg^{-1} for the inner part of the SMC and 0.05 ± 0.02 dex deg^{-1} for the outer part. The inner field MG is in excellent agreement with the field MG found by other authors in that region also using CaT (-0.075 ± 0.011 dex deg^{-1} from Dobbie et al. 2014b and -0.08 ± 0.02 dex deg^{-1} from P16). The inner cluster MG found in this work is consistent with P15 (-0.05 ± 0.04 dex deg^{-1}) considering errors, and is in excellent agreement with P22 (-0.08 ± 0.04 dex deg^{-1}). The inner cluster MG is also consistent with the inner field MG. Although these results apparently lead to the conclusion that cluster and field stars have the same MG, the dispersion for field stars considering median metallicities of field regions is very low in contrast to the high cluster metallicity dispersion, as can clearly be seen in Fig. 11, particularly in the inner region.

According to P15 and P16 two potential internal cluster groups are above and below the general field metallicity trend, which are now more clearly defined, as can be seen in Fig. 11. These two potential groups correspond to the metal-poor and metal-rich cluster groups defined in the previous section. The mean metallicity and mean age values of the two groups, with

Table 4. Gaussian mixture modeling results.

Sample	N	Unimodal fit μ (σ)	Bimodal fit μ_1 (σ_1); μ_2 (σ_2)	p value	Bimodality probability parametric bootstrap	Peaks separation	Kurtosis
All	57	−0.913 (0.180)	−0.830 (0.125); −1.106 (0.135)	0.657	39.1%	2.83 ± 0.77	−0.356
Inner	37	−0.871 (0.173)	−0.797 (0.105); −1.148 (0.061)	0.051	95.3%	4.17 ± 0.40	−0.632
Outer	20	−0.991 (0.167)	−0.959 (0.083); −1.031 (0.228)	0.611	36.6%	1.91 ± 1.69	0.314

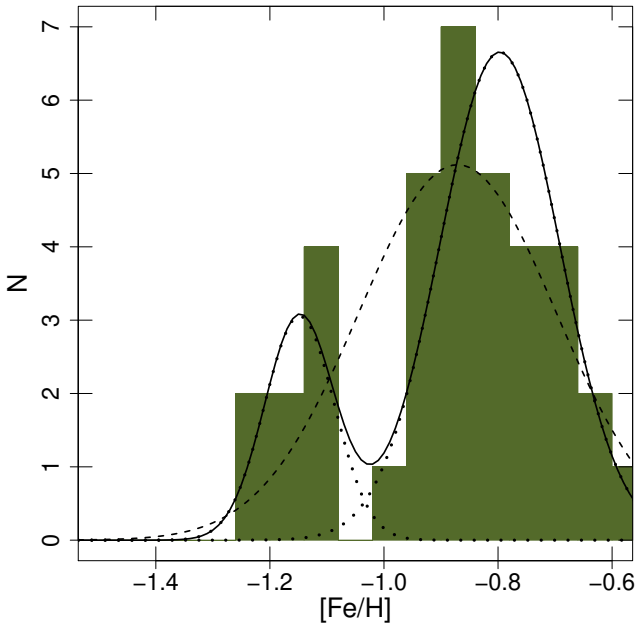

Fig. 8. Metallicity distribution of star clusters inside $a = 3.4°$. The solid, dotted and dashed lines are the same as in Fig. 7.

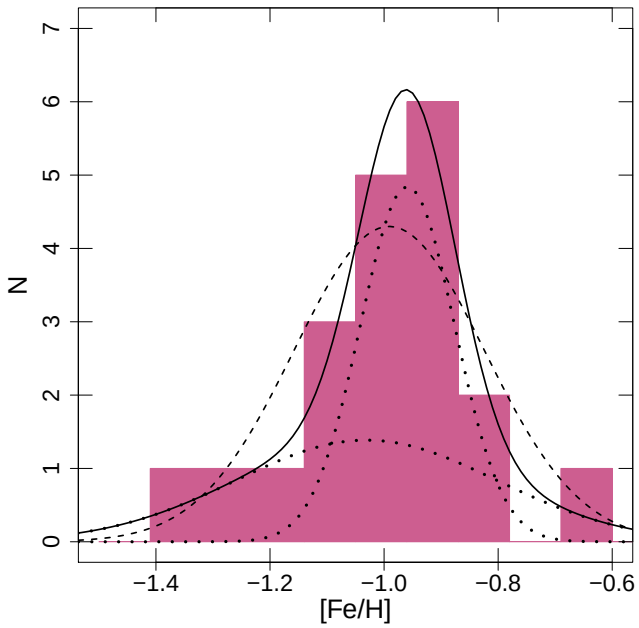

Fig. 9. Metallicity distribution of star clusters outside $a = 3.4°$. The solid, dotted and dashed lines are the same as in Fig. 7.

their respective standard deviations, are -1.15 ± 0.06 dex and 4.2 ± 3.1 Gyr for the metal-poor group, and -0.8 ± 0.10 dex and 3.1 ± 1.7 Gyr for the metal-rich group.

We performed linear fits to the two internal groups separately (dashed lines in Fig. 11, upper panel) yielding values for the MG of -0.02 ± 0.03 dex deg^{-1} and -0.003 ± 0.042 dex deg^{-1}, for the metal-rich and metal-poor groups, respectively. Within the errors, the derived values are consistent with the absence of MG in the two potential internal groups. Therefore, the MG found for the inner clusters, which is similar to that of the field stars, seems to be an artifact of the combination of two groups of clusters with a large spread in metallicity.

It is noticeable in Figs. 8 and 11 that the inner SMC lacks clusters with [Fe/H] ∼ −1.0, whereas the outer clusters have metallicities around [Fe/H] ∼ −1.0. If we assume the two groups of clusters with different origins in the inner region to be real, then we can speculate in various ways; (1) metal-rich clusters have formed in situ while the metal-poor clusters were accreted (Forbes et al. 2011), as observed in elliptical galaxies (e.g. Ennis et al. 2019; De Bórtoli et al. 2020), although the accretion mainly affects the outer part; (2) metal-poor and metal-rich gas formed clusters in the inner SMC, whereas gas with intermediate metallicity formed clusters in the SMC outskirts; (3) the SMC experienced infalls of gas with different metallicities combined with inhomogeneous mixing of gas since its formation; the multiple encounters with the LMC would have triggered cluster formation by shock.

A completely different scenario to the existence of two inner populations is to postulate that the outer clusters were formed in the SMC during a continuous cluster formation with the interstellar medium chemical enrichment and inhomogeneous mixing, but the clusters with [Fe/H] ∼ −1.0 that would be concentrated in a given inner region were moved outwards by interactions with the LMC. However, all of these possible explanations are speculative. Real distances as well as dynamical simulations must be carried out to test these or other possible scenarios.

5.3. Ages–metallicity relation

In an effort to help constrain the chemical evolution of the SMC, we plot in Fig. 12 the AMR for the full cluster sample that shows, as in our previous work, that none of the available models of chemical evolution reproduce the data adequately. If the different regions of the SMC (D16, D21) are analyzed separately, the AMR becomes somewhat clearer. The AMR of the main body, which is the region of interest of the present paper, is presented in Fig. 13. In that figure we identify with red and blue symbols the clusters belonging to the metal-rich and metal-poor groups, respectively. We compare the observational data with different models of chemical evolution (see the caption of the figure for model references).

Figure 13 shows that 21 of the 28 metal-rich clusters (75%) are concentrated at ages younger than 4−5 Gyr and none is older than about 6−7 Gyr, whereas metal-poor clusters cover a

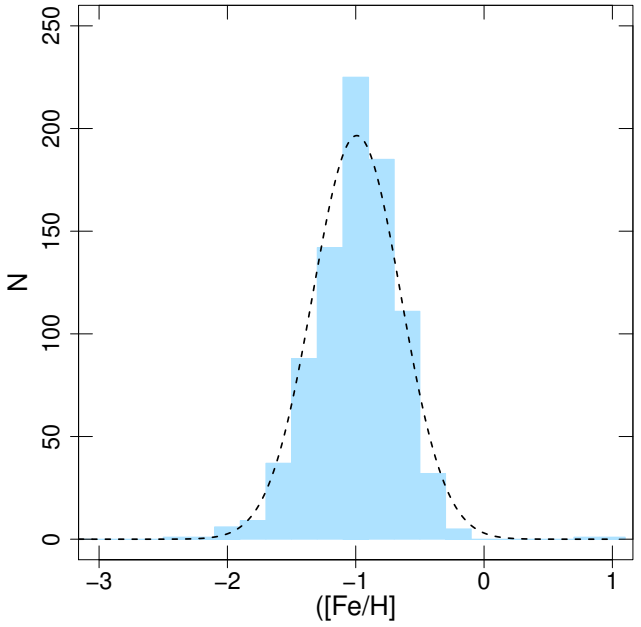

Fig. 10. Metallicity distribution of field stars. The dashed line shows a unimodal fit.

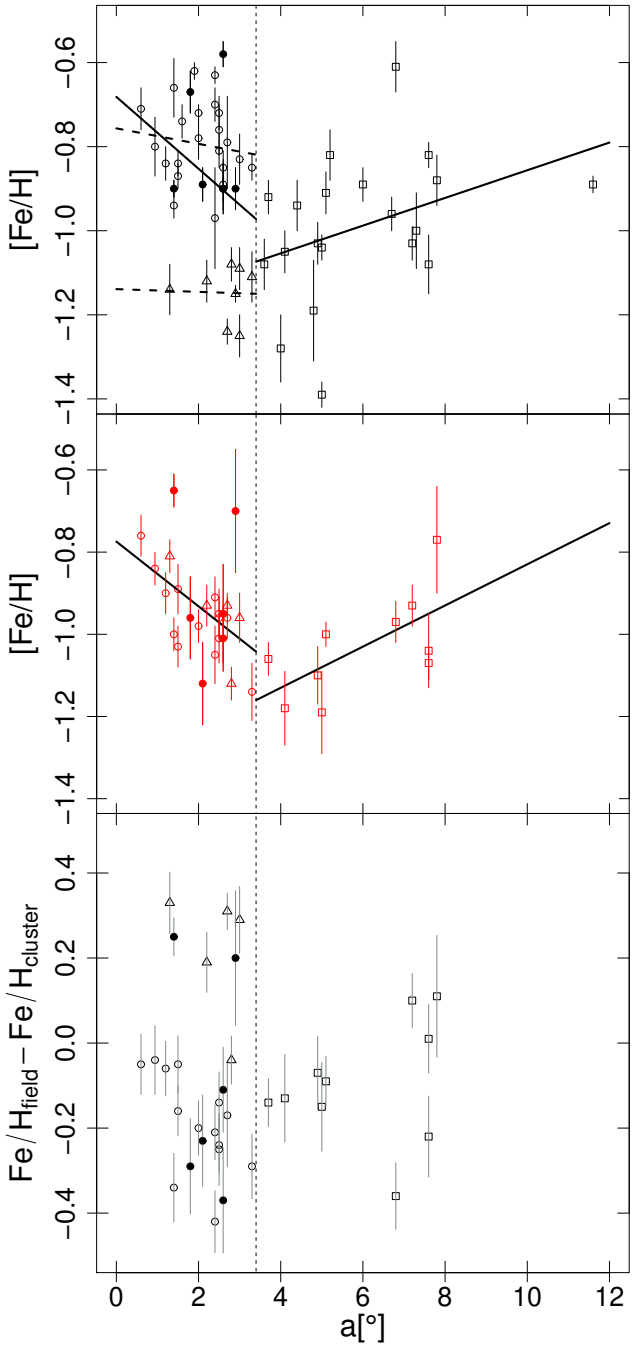

Fig. 11. Metallicity gradient for clusters (*upper panel*) and field stars (*middle panel*). *Bottom panel*: difference between field and cluster metalicities. The filled and open circles are the clusters and fields studied in this work and from the literature, respectively; the circles and triangles show the metal-rich and metal-poor groups in the inner region; the squares show the clusters in the outer region. The vertical line indicates the limit between the inner and outer regions.

wider age range, although the number of metal-poor clusters is low. The age of ∼6 Gyr corresponds approximately to the time where star formation was probably triggered by the infall to the SMC-LMC pair towards the MW (e.g., Besla et al. 2012). It is interesting to note that the age distribution of the SMC clusters shows a peak at ∼5 Gyr (Piatti et al. 2011; Parisi et al. 2014; Bica et al. 2020), which agrees with a peak in the field star formation rate of $\log(t) = 9.7$ from Rubele et al. (2018). On the other hand, while the clusters of the metal-rich group present a metallicity dispersion of ∼0.4 dex, the clusters of the metal-poor group are found concentrated in a significantly smaller metallicity range (±0.1 dex) around the previously calculated mean value of −1.15 dex. The oldest clusters of the metal-rich group show a primordial constant metallicity of -0.86 ± 0.04 dex (without considering HW41, see below) until 4−5 Gyr ago, showing a pronounced subsequent chemical enrichment process that increased the metallicity considerably, at least for about half of the younger clusters. On the contrary, metal-poor cluster formation appears not to have undergone any chemical enrichment throughout the life of the SMC, which suggests a low efficient gas mixing for the metal-poor gas that kept forming clusters during the entire life of the SMC. The chemical evolution of the metal-rich group clusters would seem to be well represented by the Harris & Zaritsky (2004, H&Z) and Perren et al. (2017) models. Particularly interesting is that the AMR proposed by H&Z was specifically derived from the star formation history (SFH) of 361 regions located in the main body of the SMC ($4° \times 4.5°$). This finding supports the arguments of D16 that each region of the SMC should be analyzed separately, possibly revealing specific pieces of the chemical evolution history of the SMC. This result also suggests a similar chemical evolution for field stars analyzed by H&Z and metal-rich star clusters analyzed here in the SMC main body region.

One exception to this apparent match with the H&Z and Perren et al. (2017) models is the cluster HW 41 for which there is a large dispersion in the age determination that can be found in the literature (marked in Fig. 13 with a rectangle). Piatti (2011a) derived an age of 6 ± 1 Gyr using the δT_1 age index in the Washington photometric system, and Parisi et al. (2014) determined an age of 5.6 ± 0.4 from the conversion of Piatti's δT_1 to δV index. On the other hand, Glatt et al. (2010) and Perren et al. (2017), applying automatic fitting methods, found age values for HW 41 of 1 Gyr and 3.8 Gyr, respectively. We adopted for our analysis the age from Parisi et al. (2014), but a more reliable age needs to be derived for this cluster.

Considering the analysis in this section and assuming that the metal-rich group corresponds to clusters formed in situ, while

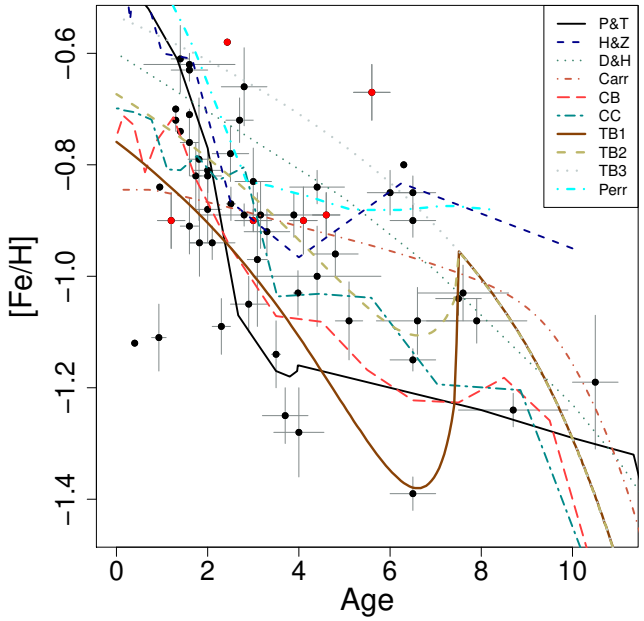

Fig. 12. Age-metallicity relation for the full cluster sample. Different AMR models are included. The clusters studied in this work and those taken from the literature are represented with red and black circles, respectively. References for the AMR models: P&T: Pagel & Tautvaisiene (1998), H&Z: Harris & Zaritsky (2004), D&H: Da Costa & Hatzidimitriou (1998), Carr: Carrera et al. (2008), CB and CC: Cignoni et al. (2013), T&B1, T&B2 and T&B3: Tsujimoto & Bekki (2009), Perr: Perren et al. (2017).

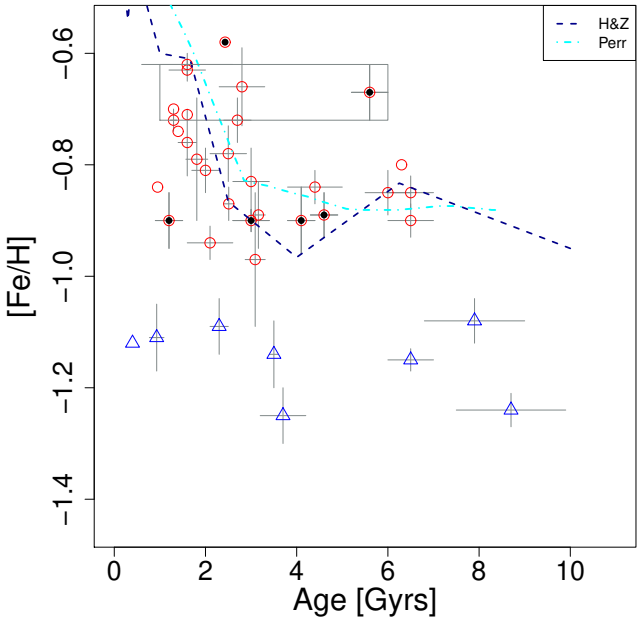

Fig. 13. Age-metallicity relation inside 3.4°. The red circles and blue triangles show clusters corresponding to the metal-rich and metal-poor groups, respectively. The six clusters studied in this work are represented with filled symbols. The references for the AMR models are the same as in Fig. 12. The cluster HW41 has been plotted within a rectangle that represents the range of ages that can be found in the literature for this cluster (see text for details).

those of the metal-poor group have a different origin, then the AMR of the SMC main body corresponds to the relation found for the metal-rich group.

6. Summary and conclusions

Using Ca II Triplet lines we determined the mean RV and metallicity of six clusters and six fields in the SMC. We added another 51 clusters and 30 fields studied with the same technique and with metallicities on the same scale. We divided our samples into inner and outer regions considering the breakpoint derived by Dias et al. (2021) (a = 3.4°). According to the definition of Dias et al. (2016, 2021) and P22, the inner region corresponds to the SMC main body. Our main conclusions are the following:

- We find a high probability (95.3%) that the cluster MD is bimodal in the inner region, but unimodal in the outer regions.
- Considering the bimodal MD in the inner region, we define two cluster groups as metal-rich and metal-poor with mean metallicities of −0.80 and −1.15 dex, respectively.
- The outer cluster MD and field MD have coincident unimodal peaks at −0.99 dex.
- The cluster metallicity gradient (MG) is negative (-0.08 ± 0.04 dex deg^{-1}) in the inner region, but positive or null in the outer region (0.03 ± 0.02 dex deg^{-1}), in agreement with the MG for field stars. However, linear fits for the metal-rich and metal-poor clusters separately are consistent with no MG. In the outer region field stars the MG is significantly positive.
- With our extended sample we continue to find the cluster metallicity gap in the main body at ∼−1, as suggested by P16.
- The age-metallicity relation (AMR) in the inner region shows that the metal-rich clusters appear to follow the chemical enrichment of field stars by Harris & Zaritsky (2004) or the model proposed by Perren et al. (2017), but metal-poor clusters do not present any chemical enrichment.

In this work we present observational evidence that the chemical enrichment is complex in the SMC main body. Two cluster groups with potentially different origins could be coexisting in the main body but more data with precise and homogeneous metallicities and distances are needed to corroborate not only the metallicity gap but also any possible projection effects. Dynamical simulations are required to understand possible different origins for the metal-rich and metal-poor cluster groups in the SMC main body.

Acknowledgements. We thank the referee for the comments that helped to improve this paper. This work was funded with grants from Consejo Nacional de Investigaciones Científicas y Técnicas de la República Argentina, Agencia Nacional de Promoción Científica y Tecnológica, and Universidad Nacional de La Plata (Argentina). This research was partially supported by the Argentinian institution SECYT (Universidad Nacional de Córdoba). Based on observations obtained at the Gemini Observatory (programme GS-2016B-Q-17, PI: M.C. Parisi), which is operated by the Association of Universities for Research in Astronomy, Inc., under a cooperative agreement with the NSF on behalf of the Gemini partnership: the National Science Foundation (United States), the National Research Council (Canada), CONICYT (Chile), the Australian Research Council (Australia), Ministério da Ciencia, Tecnologia e Inovacao (Brazil) and Ministerio de Ciencia, Tecnología e Innovación Productiva (Argentina). This work presents results from the European Space Agency (ESA) space mission *Gaia*. *Gaia* data are being processed by the *Gaia* Data Processing and Analysis Consortium (DPAC). Funding for the DPAC is provided by national institutions, in particular the institutions participating in the *Gaia* MultiLateral Agreement (MLA). The *Gaia* mission website is https://www.cosmos.esa.int/gaia. The *Gaia* archive website is https://archives.esac.esa.int/gaia. This research has made use of "Aladin sky atlas" developed at CDS, Strasbourg Observatory, France. D.G. gratefully acknowledges support from the ANID BASAL project ACE210002. D.G. also acknowledges financial support

from the Dirección de Investigación y Desarrollo de la Universidad de La Serena through the Programa de Incentivo a la Investigación de Académicos (PIA-DIDULS). B.D. acknowledges support by ANID-FONDECYT iniciación grant No. 11221366.

References

Armandroff, T. E., & Da Costa, G. S. 1991, AJ, 101, 1329
Armandroff, T. E., & Zinn, R. 1988, AJ, 96, 92
Ashman, K. M., Bird, C. M., & Zepf, S. E. 1994, AJ, 108, 2348
Bekki, K., & Chiba, M. 2007, PASA, 24, 21
Belokurov, V. A., & Erkal, D. 2019, MNRAS, 482, L9
Besla, G., Kallivayalil, N., Hernquist, L., et al. 2007, ApJ, 668, 949
Besla, G., Kallivayalil, N., Hernquist, L., et al. 2010, ApJ, 721, L97
Besla, G., Kallivayalil, N., Hernquist, L., et al. 2012, MNRAS, 421, 2109
Besla, G., Martínez-Delgado, D., van der Marel, R. P., et al. 2016, ApJ, 825, 20
Bica, E., Westera, P., Kerber, L. D. O., et al. 2020, AJ, 159, 82
Bitsakis, T., González-López lira, R. A., Bonfini, P., et al. 2018, ApJ, 853, 104
Carrera, R., Gallart, C., Aparicio, A., et al. 2008, AJ, 136, 1039
Choudhury, S., Subramaniam, A., Cole, A. A., & Sohn, Y. J. 2018, MNRAS, 475, 4279
Choudhury, S., de Grijs, R., Rubele, S., et al. 2020, MNRAS, 497, 3746
Cignoni, M., Cole, A. A., Tosi, M., et al. 2013, ApJ, 775, 83
Cioni, M. R. L. 2009, A&A, 506, 1137
Coelho, P. R. T. 2014, MNRAS, 440, 1027
Cole, A. A., Smecker-Hane, T. A., Tolstoy, E., Bosler, T. L., & Gallagher, J. S. 2004, MNRAS, 347, 367
Connors, T. W., Kawata, D., & Gibson, B. K. 2006, MNRAS, 371, 108
Da Costa, G. S. 1991, in The Magellanic Clouds, eds. R. Haynes, & D. Milne, 148, 183
Da Costa, G. S., & Hatzidimitriou, D. 1998, AJ, 115, 1934
De Bórtoli, B. J., Bassino, L. P., Caso, J. P., & Ennis, A. I. 2020, MNRAS, 492, 4313
De Leo, M., Carrera, R., Noël, N. E. D., et al. 2020, MNRAS, 495, 98
Dias, B., & Parisi, M. C. 2020, A&A, 642, A197
Dias, B., Kerber, L. O., Barbuy, B., et al. 2014, A&A, 561, A106
Dias, B., Kerber, L., Barbuy, B., Bica, E., & Ortolani, S. 2016, A&A, 591, A11
Dias, B., Angelo, M. S., Oliveira, R. A. P., et al. 2021, A&A, 647, L9
Dias, B., Parisi, M. C., Angelo, M., et al. 2022, MNRAS, 512, 4334
Diaz, J., & Bekki, K. 2011, MNRAS, 413, 2015
Diaz, J. D., & Bekki, K. 2012, ApJ, 750, 36
Dobbie, P. D., Cole, A. A., Subramaniam, A., & Keller, S. 2014a, MNRAS, 442, 1663
Dobbie, P. D., Cole, A. A., Subramaniam, A., & Keller, S. 2014b, MNRAS, 442, 1680
D'Onghia, E., & Fox, A. J. 2016, ARA&A, 54, 363
Dopita, M. A., Vassiliadis, E., Wood, P. R., et al. 1997, ApJ, 474, 188
El Youssoufi, D., Cioni, M.-R. L., Bell, C. P. M., et al. 2021, MNRAS, 505, 2020
Ennis, A. I., Bassino, L. P., Caso, J. P., & De Bórtoli, B. J. 2019, MNRAS, 488, 770
Forbes, D. A., Spitler, L. R., Strader, J., et al. 2011, MNRAS, 413, 2943
Gaia Collaboration (Brown, A. G. A., et al.) 2018, A&A, 616, A1
Gaia Collaboration (Luri, X., et al.) 2021, A&A, 649, A7
Gardiner, L. T., & Noguchi, M. 1996, MNRAS, 278, 191
Gimeno, G., Roth, K., Chiboucas, K., et al. 2016, in Ground-based and Airborne Instrumentation for Astronomy VI, eds. C. J. Evans, L. Simard, & H. Takami, SPIE Conf. Ser., 9908, 99082S
Glatt, K., Grebel, E. K., & Koch, A. 2010, A&A, 517, A50
Graczyk, D., Pietrzyński, G., Thompson, I. B., et al. 2020, ApJ, 904, 13
Hanuschik, R. W. 2003, A&A, 407, 1157
Harris, J., & Zaritsky, D. 2004, AJ, 127, 1531
Hook, I. M., Jørgensen, I., Allington-Smith, J. R., et al. 2004, PASP, 116, 425
Kallivayalil, N., van der Marel, R. P., Besla, G., Anderson, J., & Alcock, C. 2013, ApJ, 764, 161
Maia, F. F. S., Dias, B., Santos, J. F. C., et al. 2019, MNRAS, 484, 5702
Martin, G., Jackson, R. A., Kaviraj, S., et al. 2021, MNRAS, 500, 4937
Mathewson, D. S., Cleary, M. N., & Murray, J. D. 1974, ApJ, 190, 291
Mauro, F. 2020, in Astronomical Data Analysis Software and Systems XXVII, eds. P. Ballester, J. Ibsen, M. Solar, & K. Shortridge, ASP Conf. Ser., 522, 699
Mauro, F., Moni Bidin, C., Chené, A. N., et al. 2013, Rev. Mex. Astron. Astrofis., 49, 189
Mayer, L., Governato, F., Colpi, M., et al. 2001, ApJ, 559, 754
Muratov, A. L., & Gnedin, O. Y. 2010, ApJ, 718, 1266
Narloch, W., Pietrzyński, G., Gieren, W., et al. 2021, A&A, 647, A135
Nayak, P. K., Subramaniam, A., Choudhury, S., Indu, G., & Sagar, R. 2016, MNRAS, 463, 1446
Nayak, P. K., Subramaniam, A., Choudhury, S., & Sagar, R. 2018, A&A, 616, A187
Nidever, D. L., Majewski, S. R., & Butler Burton, W. 2008, ApJ, 679, 432
Nidever, D. L., Majewski, S. R., Butler Burton, W., & Nigra, L. 2010, ApJ, 723, 1618
Nidever, D. L., Price-Whelan, A. M., Choi, Y., et al. 2019, ApJ, 887, 115
Niederhofer, F., Cioni, M. R. L., Rubele, S., et al. 2018, A&A, 613, L8
Niederhofer, F., Cioni, M.-R. L., Rubele, S., et al. 2021, MNRAS, 502, 2859
Olszewski, E. W., Schommer, R. A., Suntzeff, N. B., & Harris, H. C. 1991, AJ, 101, 515
Pagel, B. E. J., & Tautvaisiene, G. 1998, MNRAS, 299, 535
Parisi, M. C., Grocholski, A. J., Geisler, D., Sarajedini, A., & Clariá, J. J. 2009, AJ, 138, 517
Parisi, M. C., Geisler, D., Grocholski, A. J., Clariá, J. J., & Sarajedini, A. 2010, AJ, 139, 1168
Parisi, M. C., Geisler, D., Carraro, G., et al. 2014, AJ, 147, 71
Parisi, M. C., Geisler, D., Clariá, J. J., et al. 2015, AJ, 149, 154
Parisi, M. C., Geisler, D., Carraro, G., et al. 2016, AJ, 152, 58
Parisi, M. C., Gramajo, L. V., Geisler, D., et al. 2022, A&A, 662, A75
Patel, E., Besla, G., & Sohn, S. T. 2017, MNRAS, 464, 3825
Perren, G. I., Piatti, A. E., & Vázquez, R. A. 2017, A&A, 602, A89
Piatek, S., Pryor, C., & Olszewski, E. W. 2008, AJ, 135, 1024
Piatti, A. E. 2011a, MNRAS, 416, L89
Piatti, A. E. 2011b, MNRAS, 418, L69
Piatti, A. E. 2018, MNRAS, 478, 784
Piatti, A. E., Santos, J. F. C., Jr., Clariá, J. J., et al. 2005, A&A, 440, 111
Piatti, A. E., Clariá, J. J., Bica, E., et al. 2011, MNRAS, 417, 1559
Pietrzyński, G., Graczyk, D., Gallenne, A., et al. 2019, Nature, 567, 200
Putman, M. E., Staveley-Smith, L., Freeman, K. C., Gibson, B. K., & Barnes, D. G. 2003, ApJ, 586, 170
Rubele, S., Pastorelli, G., Girardi, L., et al. 2018, MNRAS, 478, 5017
Rutledge, G. A., Hesser, J. E., Stetson, P. B., et al. 1997a, PASP, 109, 883
Rutledge, G. A., Hesser, J. E., & Stetson, P. B. 1997b, PASP, 109, 907
Santos, J. F. C., Jr., Maia, F. F. S., Dias, B., et al. 2020, MNRAS, 498, 205
Tsujimoto, T., & Bekki, K. 2009, ApJ, 700, L69
Vásquez, S., Zoccali, M., Hill, V., et al. 2015, A&A, 580, A121
Whitmore, B. C., Zhang, Q., Leitherer, C., et al. 1999, AJ, 118, 1551
Zivick, P., Kallivayalil, N., van der Marel, R. P., et al. 2018, ApJ, 864, 55